Systemic inflammation reduces astrocyte Ca^{2+} and neurovascular coupling in a mouse model of Alzheimer's disease

Chang Liu, Kimia Abdolhosseini Sakha, Jaime Anton, Alfredo Cardenas-Rivera, Mohammad A. Yaseen

ABSTRACT

Neuroinflammation and neurovascular dysfunction are two major pathologies in Alzheimer's disease (AD), yet their interplay remains poorly understood. Astrocytes are central players in both brain immunity and neurovascular coupling. In this study, we induced neuroinflammation through systemic administration of lipopolysaccharide (LPS) in 12-month-old APP/PS1dE9 mice and simultaneously monitored the astrocyte Ca^{2+} signaling and the brain hemodynamics with two-photon microscopy. We showed that the spontaneous release of Ca^{2+} in astrocytes was elevated in AD mice and decreased by 14 days of LPS administration. The effects of LPS-induced inflammation on astrocytic Ca^{2+} signaling varied substantially between brief 3 sensory stimulation and sustained 30 second sensory stimulation with modest effects on vascular responses. These findings highlight the nuanced impact of neuroinflammation on astrocytic Ca^{2+} dynamics and brain hemodynamics in AD, shedding light on mechanisms that link these pathologies.

Keywords: Alzheimer's disease, neuroinflammation, lipopolysaccharide, astrocyte Ca^{2+}, neurovascular coupling, two-photon microscopy

Author affiliations:
1 Department of Bioengineering, Northeastern University, Boston, MA 02115, USA

Correspondence:
Mohammad Abbas Yaseen
Northeastern University BIOE,
360 Huntington Ave, ISEC 206
Boston, MA 02115
m.yaseen@northeastern.edu

1. INTRODUCTION

Neuroinflammation and neurovascular dysfunction are two major pathologies in Alzheimer's disease (AD) [1–4]. These pathologies share cellular components, with astrocytes playing a vital role in both brain immunity and neurovascular coupling [5,6]. Under inflammatory conditions, astrocytes become activated, undergoing phenotypic and morphological changes that facilitate the release of cytokines. The reactive astrocytes contribute to amyloid beta pathology and neural network dysfunction [7,8]. Studies showed altered astrocyte Ca^{2+} signaling in reactive astrocytes [9,10]. Additionally, astrocyte Ca^{2+} signaling also regulates cerebral blood flow [6]. Thus, investigating astrocytic Ca^{2+} signaling and cerebrovascular function under inflammatory conditions will provide insights into the relationship between neuroinflammation and neurovascular dysfunction in Alzheimer's disease. Previous studies showed systemic inflammation disrupts cerebral hemodynamics in healthy rodent brains and human patients with small vessel disease and traumatic brain injury [11–13]. Systemic injection of the bacteria-derived endotoxin lipopolysaccharide (LPS) has been used as a model to study neuroinflammation in neurodegenerative disease [14]. Peripheral inflammation induced by systemic injection of LPS can transfer to the central nervous system and cause a prolonged inflammatory response in the brain [15]. Here, we subjected the 12-month-old female APPswe/PS1dE9 mice and their wildtype littermates (n=8 each) to two weeks of LPS-induced systemic inflammatory threat and measured cerebral vessel dynamics and astrocyte Ca^{2+} release during functional brain activation using two-photon microscopy.

2. METHODS

2.1 Animal preparation

All experiments were performed following ARRIVE guidelines for animal care, under a protocol approved by the Northeastern University Institutional Animal Care and Use Committee. The mouse strain used for this research project, B6C3-Tg(APPswe,PSEN1dE9)85Dbo/Mmjax, RRID:MMRRC_034829-JAX, was obtained from the Mutant Mouse Resource and Research Center (MMRRC) at The Jackson Laboratory, an NIH-funded strain repository, and was donated to the MMRRC by David Borchelt, Ph.D., McKnight Brain Institute, University of Florida. The double transgenic AD mouse co-expresses the Swedish mutation of amyloid precursor protein (APP) and a mutant human presenilin 1 gene (PS1-dE9) and accumulates beta-amyloid deposits in the cortex at 6 months [Jankowski 2004]. The study used female APP/PS1dE9 mice and their wild-type littermates (age 12-13 months, n=8 per cohort) [1]. At 10 months of age, mice underwent cranial window surgery followed by GFAP-promoted GCaMP6f virus injection. Under isoflurane anesthesia (3–3.5%

isoflurane for induction and 1–2% for maintenance), hair and skin was removed to expose the skull, and a titanium butterfly-shaped head post was implanted using dental cement [17]. After the localization of the injection site, a ~ 3 mm diameter of cranial window was created on the barrel cortex of the mouse, followed by targeted injection of a GFAP-promoted GCaMP6f virus (pZac2.1gfaABC1D-cyto-GCaMP6f, Plasmid #52925, Addgene). Virus (300–500 nL) was injected at 2 nL/s, 300–350 μm below the brain surface, using a glass micropipette and a Nanoinjector III (Drummond Scientific) [18]. Injections were performed in two to three cortical regions to increase the area of viral expression. The procedure lasted 15 to 20 minutes, with the dura kept hydrated throughout. After the injections, the dura was covered with a CNC-machined transparent acrylic coverslip (outer diameter: 5 mm, inner diameter: 3 mm). The mouse was then removed from the stereotaxic frame and allowed to recover from anesthesia. The animal was single-housed and provided with 5 days of post-operative care (40/8 mg/ml, sulfametoxazole/trimethiporim (SMX-TMP) in drinking water). Buprenorphine (0.05 mg/kg at 0.03 mg/ml) was administered subcutaneously for three days after surgery. To label astrocytes in the activation center, we conducted optical intrinsic signal imaging (OISI) and whisker stimulation on the anesthetized mouse before removing the skull. The skull over the barrel cortex (A-P: 2mm, M-L: 3 mm) was thinned, and whiskers on the contralateral side of the thinned skull were deflected using a cotton swab. The skull was illuminated with an LED light source during the stimulation through a green bandpass filter (568/10 nm). The reflected light was recorded with a CMOS camera (Basler acA1300–200μm, Edmund optics) mounted on the surgical microscope, and the relative intensity change was calculated with a customized MATLAB script. Regions with the greatest intensity drop were identified as the activation area and selected as the site for viral injection.

2.2 Habituation training

Headpost restraint training started 7 to 10 days post-surgery using a custom-made imaging cradle. During training, the mouse was conditioned to tolerate head immobilization from 5 minutes to 1 hour. Whisker stimulation was included during the final training sessions to acclimate the animal to the functional activation experiment. Milk was given as a reward during the training.

2.3 Systemic inflammation induction

Systemic inflammation was induced through daily intraperitoneal (i.p.) injections of 0.3 mg/kg lipopolysaccharide (LPS, *E. coli* O55: B5, L4005, CAS-No. 93572-42-0, Sigma-Aldrich) for 14 days. A stock solution of LPS was prepared at 1mg/mL in phosphate-buffered saline (PBS) and stored at -20°C. The solution was vortexed and diluted 4-fold to 0.25 mg/mL for each injection.

62 **2.4 Functional activation protocol**

63 A capillary tube with a 3D-printed broom-like end was positioned approximately 2.5–3 cm from the nose,
64 parallel to the right side of the mouse's face, and below the eye to avoid directing air toward the eyes during
65 stimulation. Air puffs were delivered through the tube and controlled using a pneumatic drug injection system
66 (PDES-DXH, ALA Scientific, USA). Two whisker stimulation protocols—brief and prolonged—were
67 performed. The brief protocol consisted of a 5-second baseline, 2.7 seconds of 1.67 Hz stimulation (5 pulses,
68 20 psi), and 22.3 seconds of recovery. The prolonged protocol included a 5-second baseline, 30 seconds of 1.67
69 Hz stimulation (50 pulses, 20 psi), and 30 seconds of recovery. Short and long stimulations were interleaved
70 within each trial and repeated 10 times.

71 **2.5 Functional activation center mapping**

72 The activation center of whisker stimulation was mapped using optical intrinsic signal imaging (OISI) under
73 the brief whisker stimulation protocol. A white LED illuminator (SCHOTT KL 1600) with a 568/10 nm
74 bandpass filter (Edmund Optics) served as the light source. The camera was triggered by a TTL signal from a
75 general-purpose input/output (GPIO) hardware trigger. A fiber-optic LED light source illuminator (SCHOTT
76 KL 1600 LED) delivered light to the cranial window at a 60° angle. Reflected light was collected using a 4×
77 objective (Nikon Instruments Inc.) and recorded at 5 Hz for 20 seconds with a CMOS camera (Basler acA1300–
78 200μm, Edmund Optics). Baseline intensity (I_0) was calculated by averaging the intensity over the baseline
79 recording. Relative intensity (I/I_0) was calculated for all imaging frames. Cortical area with the maximal
80 intensity decreases was identified as the activation center.

81 **2.6 Two-photon imaging in awake mice**

82 Two-photon imaging of astrocyte Ca^{2+} signaling and vascular dynamics at barrel cortex at resting-state and
83 during functional activation was conducted using the multiphoton imaging system Ultima2pPlus (Bruker Nano,
84 Inc) with a 25× objective (1.10 NA, Nikon Instruments Inc). Imaging during the functional activation
85 experiment was synchronized with the whisker stimulation protocol. Blood vessels were labeled through retro-
86 orbital injection of Texas Red Dextran (2.5% w/v, 80uL). A tunable ultrafast laser (InSight X3+, Spectral-
87 Physics) was tuned to 940 nm for simultaneous imaging of blood vessels and astrocytic Ca^{2+} imaging. We
88 tracked the penetrating arterioles from the pial surface to the deepest assessable cortical layer and recorded the
89 vessel diameter and the astrocyte Ca^{2+} release using a minimal frame rate of 4.3 Hz. The image field of view
90 (FOV) was around $88 \times 88\, um^2$. On the following day, capillary diameter and red blood cell velocity in
91 response to the interleaved functional activation was measured with two-photon line scanning [19], with a scan
92 frequency ranging from 369.87 to 1034.8 Hz. Angiogram and z-stacks of GCaMP6f-expressing astrocytes (0–
93 350 μm below the pial surface) were taken at the end of the experiment. Penetrating arterioles perpendicular to

the image plane and capillaries parallel to it were selected to ensure accurate diameter estimation, while tilted vessels were excluded during post-processing. We measured regions from 49 to 414 μm below the pial surface for WT mice and 30 to 360 μm below the pial surface for AD mice.

2.7 Two-photon imaging data analysis

Astrocyte Ca^{2+}: Image frames were pre-processed using a non-rigid motion correction algorithm [20], followed by median filtering. Resting-state astrocyte Ca^{2+} fluctuations were quantified using a region-of-interest-based Ca^{2+} analysis tool: "GECIquant" in ImageJ [21]. Briefly, average intensity projection was generated from the time series of two-photon raster scan images. We created a binary region of interest (ROI) mask where the area within the polygon ROI is set to 1 and the rest of the image is set to 0. Mean intensity within the ROI over time was calculated. The area criterion was set to 30 μm^2 to Inf for astrocyte soma and endfeet, and 8 to 2000 μm^2 for Ca^{2+} waves in processes. Relative intensity change ($\Delta F/F_0 = (F_t - F_0)/F_0 \times 100$) was calculated. F_0 was calculated as the median of the lowest 5% fluorescence intensity over the entire 10-minute raster scan. $\Delta F/F_0$ of all astrocyte ROIs from all mice were interpolated with a $\mathrm{d}t = 0.2244\ s$, (i.e., 4.45 fps). The $\Delta F/F_0$ traces were pre-processed using linear detrending to remove intensity drift that occurred during the measurement. The detrended intensity traces were then low pass filtered with a cutoff frequency of 0.1 Hz, as determined by power spectrum analysis. To determine the threshold for the Ca^{2+} event, we reviewed our data and found that the frequency of Ca^{2+} events within all three astrocyte ROIs (soma, endfeet, and process) is less than one event per min per ROI. Assuming each event lasted 10 seconds, more than 80% of the 10-minute recording were 'eventless'. Therefore, we calculated the median absolute deviation (MAD) of the lowest 80% of the $\Delta F/F_0$ trace and used 5 times the MAD as the threshold for the Ca^{2+} event. This threshold is more robust to outliers compared to the conventional standard deviation approach and reduces the number of 'false positives'. Ca^{2+} events were detected and quantified using the 'findpeaks' function in MATLAB. The detected events were categorized as either 'singlepeak' or 'multipeak' events as described [22]. Finally, we calculated the frequency of the event as per min per ROI. Ca^{2+} release during whisker stimulation was quantified as $\Delta F/F_0$. F_0 was calculated as the average intensity during the first 5 seconds of the resting-state recording.

Arteriole diameter: Arteriole diameter in response to functional activation was quantified using the automatic structure tracking algorithm developed by Haidey et al. [23]. The algorithm tracks the cross-sectional area of the vessel based on user-defined luminal edges. Vessel diameter (D) was calculated from the cross-sectional area. Relative change of diameter ($\Delta D/D_0 = (D_t - D_0)/D_0 \times 100$) was calculated, where the baseline diameter (D_0) was the average diameter over the 5-second resting-state measurement. Since the frame rates of different imaging fields can sometimes vary slightly, $\Delta D/D_0$ were interpolated with $\Delta t = 0.2244\ s$.

125 $\Delta D/D_0$, $\Delta F/F$ *quantification:* We first quantified response in penetrating arteriole (p.a.) and the Ca^{2+} release
126 in astrocyte endfeet wrapped around the p.a. Stimulation trials were categorized into four groups: (1) trials with
127 both arteriole dilation and astrocyte endfeet Ca^{2+} increase, (2) trials with only arteriole dilation, (3) trials with
128 only astrocyte endfeet Ca^{2+} release, and (4) trials with no response in either. Trials with motion artifacts were
129 excluded. To analyze the correlation between arteriole dilation and astrocyte endfeet $Ca^{2+,}$ we calculated the
130 average arteriole dilation and Ca^{2+} release in trials where both responses were observed. The averaged arteriole
131 dilation and Ca^{2+} release were then low-pass filtered with a cutoff frequency of 0.2Hz. Amplitude and kinetics
132 of the vascular response and Ca^{2+} release were characterized using the 'findpeaks' function in MATLAB. For
133 30s whisker stimulation, we also evaluate the average response during the last 2s of the stimulation. Average
134 Ca^{2+} signaling in astrocyte soma and processed were calculated over the selected stimulation trials.

135 *Capillary diameter:* Space-time images from two-photon line scans were denoised using a 2D median filter.
136 Vessel diameter was calculated using the MATLAB two-photon imaging analysis toolbox, CHIPS [24]. The
137 algorithm normalizes the vessel's intensity profile to a range of 0 to 1 and calculates the diameter using the full
138 width at a user-defined height. We used the full width at 0.4 of the maximum intensity, as it provided the most
139 accurate diameter estimation based on our signal-to-background ratio. The sampling rate was set at a maximum
140 of 20 Hz. Measurements affected by motion, particularly along the axial axis were discarded. The average
141 diameter and $\Delta D/D_0$ across all selected stimulation trials were calculated. The $\Delta D/D_0$ traces were smoothed
142 using a moving median filter with a one-second window (20 data points). Vascular dilation amplitude and
143 kinetics were analyzed using the same method as in raster-scan data analysis. Vessels were categorized by
144 branch order: 0th-order penetrating arterioles, 1st and 2nd-order capillaries, and higher-order capillaries (3rd-order
145 branches and above).
146 *Capillary RBC velocity*: The space-time images were filtered using Sobel filtering, and the capillary red blood
147 cell (RBC) velocity was analyzed using the iterative Radon Transform [25]. Image segments of every 100 lines
148 were used to calculate RBC velocity, velocity at the next time point was calculated after skipping 25 lines.
149 $\Delta v/v_0$ was calculated and smoothed using a moving median filter.
150

151 **2.8 Tissue collection and immunofluorescence imaging (IF)**

152 After 14 days of LPS treatment, mice were sacrificed, and brains were collected for immunofluorescence (IF)
153 staining. IF staining was performed on a subset of the imaged mice (n=3 per cohort). Mice received 14 days of
154 saline injections at a volume equivalent to the LPS dose of 0.3 mg/kg served as control group (n=2 for WT,
155 n=3 for AD). Mice were intracardially perfused with 40 mL of heparin-PBS solution, followed by 20 mL of
156 4% paraformaldehyde (PFA) for fixation. The brains were collected and stored in 4% PFA for a maximum of

24 hours, then transferred to 70% ethanol and stored in -4 ℃. The brain samples were sent to the Dana-Farber/Harvard Cancer Center Specialized Histopathology Services Core (Boston, MA, USA) for immunofluorescence staining. The samples were paraffin-embedded and sliced into approximately 10 μm thick sections for IF staining. Nuclei were stained with DAPI, microglia with an anti-Iba-1 antibody labeled with Alexa Fluor 594, and astrocytes with an anti-GFAP antibody labeled with Alexa Fluor 647. IF images were collected with confocal microscopy (LSM 800, ZEISS). DAPI, AF-647, and AF-594 were excited with 405nm, 640nm, and 561nm, respectively. Images were taken using $5\times$ and $10\times$ objectives. Barrel cortex and hippocampus were identified using the Allen Brain Atlas. For each 10× field of view ($638 \times 638\, um^2$), Z-stack images were collected with a step size of $0.34\ \mu m$. All images were acquired using consistent excitation power and emission detector gain settings. $A\beta_{1\text{-}42}$ was stained with anti-$A\beta_{1\text{-}42}$ antibody conjugated to Alexa Fluor 647. Fluorescence images of $A\beta_{1\text{-}42}$ were acquired with wide-field fluorescence microscopy (Zeiss Axio Observer). All images were acquired using a consistent exposure time.

2.9 IF imaging quantification

GFAP and Iba-1 expression were quantified using the maximum intensity projection (MIP) of the z-series images. Background was removed and MIP images were binarized using an intensity threshold. The percentage area of pixels with intensity above the intensity threshold was calculated. Similarly, percentage area of $A\beta_{1\text{-}42}$ load in cortex and hippocampus was quantified in Image J.

2.10 Statistical analysis

We performed statistical tests to see if there is difference in baseline astrocyte Ca2+ dynamics, stimulus-evoked vessel dilation and astrocyte Ca2+ release in AD, and how LPS affect these parameters in both WT and AD cohorts. Differences between WT and AD group before LPS injection were tested using the Wilcoxon rank sum test. Effect of LPS on both cohorts were tested using linear mixed effect model with the 'lme4' package in RStudio. Time (i.e., day0, day 7 and day14) was set as the fixed effect. And the initial value, i.e., parameter measured at day 0 of each subject were set as the random effect. Pair-wise comparison was conducted with Tukey's method in the 'emmeans' package. * = $p<0.05$, ** = $p<0.01$, ***=$p<0.001$, ****=$p<0.0001$.

185 ## 3. RESULTS

186 Among its many functions, astrocyte Ca2+ is an important mediator of neurovascular coupling [6]. Previous
187 studies reported activated astrocytes and increased astrocyte spontaneous release of Ca2+ in the
188 APPswe/PS1dE9 mice cortex. To determine whether astrogliosis affects astrocyte Ca2+-mediated contributions
189 to cerebral blood flow regulation, we measured astrocyte Ca2+ dynamics and microvascular dilation under
190 resting-state conditions and during functional hyperemia in the awake APPswe/PS1dE9 mice brain at age 12-
191 to 13-months. We then explored if a 14-day LPS-induced neuroinflammation challenge alters astrocyte calcium
192 signaling and its contributions to neurovascular coupling.

193 Recent studies demonstrate that astrocyte Ca2+ contributes significantly to sustaining functional hyperemia in
194 response to prolonged, but not brief, periods of cortical stimulation [26]. Motivated by these findings, we used
195 two-photon imaging to measure brain hemodynamics and astrocyte Ca2+ release in response to both brief (3s)
196 and sustained (30s) whisker stimulation.

197 Measurements were performed in cortical layers I and IV. Analysis via linear mixed effects model revealed no
198 significant differences between cortical layers. As a result, the data from both layers were combined.

199

200 ### 3.1 Pre-inflammation: Hyperactive astrocytes and reduced stimulus-evoked astrocyte Ca2+ in AD
201 mice

202 We first evaluated resting-state spontaneous cortical astrocyte Ca2+ by imaging GCaMP6f-labelled astrocytes
203 in awake mice. Raster scanning was performed in ~88 μm cortical regions surrounding penetrating arterioles
204 for 10 min at ~ 4.4 Hz. Dynamic Ca2+ transients were quantified and analyzed from the soma, processes, and
205 endfoot compartments of astrocytes. In AD mice, we observed ~15 – 40% higher frequencies of Ca^{2+} spikes
206 compared to age-matched wildtype littermates, with significantly higher Ca2+ frequency in the soma and
207 process compartments (Fig. 1B-C, left, p-val = 0.03 soma, p-val = 0.048 processes). No differences in the Ca2+
208 amplitudes were observed between AD and WT mice. Compared to WT littermates, the mean duration of the
209 astrocytic Ca2+ spikes in AD mice was significantly lower (26 %, p-val < 1e-4) in astrocyte processes. Shorter
210 Ca2+ durations were also observed in the soma and endfoot compartments in AD mice; however, the
211 differences were not significant. (Fig. 1C).

212 Next, we investigated whether amyloid pathology impacts functional hyperemia. We first applied optical
213 intrinsic signal imaging (OISI) during a 3 s whisker stimulus to locate the activation center (fig 1.D). We
214 measured astrocyte Ca2+ dynamics and diameter of penetrating arterioles while stimulating the mouse barrel
215 cortex via pneumatic whisker deflection. Our OISI measurement revealed slight, but not significant, differences

216 in peak cerebral blood volume response (< -1%) in AD mice relative to WT (Fig. 1C). The activated region
217 was then imaged via TPM using both raster scanning (4.4 Hz, fig 1.E) and rapid line scanning (~360 – 100 Hz,
218 downsampled to 20 Hz).

219 In response to a short ~3s functional stimulus, AD and WT mice demonstrated different responses for arterial
220 dilation and $Ca2^{+}$ signaling within astrocyte compartments. In WT mice, the area under the curve (AUC) for
221 arterial dilation response was significantly higher in WT mice (40% difference, p = 0.029), while arterial peak
222 dilation, rise times, and latency were similar between cohorts (Fig.1F and supplementary figure 1). Astrocyte
223 Ca2+ kinetics vary in different cell compartments, as reported previously. Peak amplitudes of stimulus-induced
224 Ca2+ release in AD mice appeared higher in all astrocyte compartments compared to WT mice; however, the
225 differences were not statistically significant (Fig. 1 G-I, soma p = 0.23, endfeet p = 0.21, processes p= 0.054).
226 AD mice demonstrated significantly shorter Ca^{2+} responses in astrocytic endfeet (supplementary figure 1, p =
227 7e-4). In both cohorts, we consistently observed that the short 3s whisker stimulus evoked slower astrocyte
228 Ca2+ responses relative to the vascular response. Arterioles dilated to their maximum approximately 2,1
229 seconds after the stimulus onset, while all astrocyte Ca2+ responses achieved their maximal values
230 approximately 1-1.5 s after stimulus cessation. While the slower response times in astrocytes support earlier
231 studies that downplay contributions of astrocyte Ca2+ to neurovascular coupling, our results indicate that
232 indicate astrocytes in the AD mice brain respond slightly faster and more pronouncedly than WT mice to a
233 brief sensory stimulus.

234 A longer 30s whisker stimulus yielded more striking differences between AD and WT mice, particularly in
235 astrocyte Ca2+ dynamics. Response profiles exhibited biphasic features for both arterial dilation and astrocyte
236 Ca2+ release - including a rapid rising phase followed by a prolonged plateau phase. Consequently, we analyzed
237 dilation and Ca2+ release both over the full stimulus duration (all 30 seconds) as well as the late phase (the
238 final 2 seconds). Again, AD and WT mice experienced comparable peak diameter in arterioles. Following peak
239 dilation, arterioles constricted slightly and plateaued to a slightly smaller diameter (Fig. 1 J). For both phases
240 of the 30s stimulus, we observed no significant differences in arterial dilation rise times, maximal diameter, or
241 AUC between AD and WT mice. However, following stimulus cessation, we observed significantly faster
242 constriction to baseline diameter in AD mice (supplementary Figure 1, Δt = 5.04s, p = 0.03). Astrocyte Ca2+
243 responses differed more substantially between cohorts for the 30 s stimulus (Fig 1 K-M). In WT mice, astrocytes
244 persistently release Ca2+ from all compartments until the stimulus cessation, while Ca2+ release in AD
245 astrocyte peaked rapidly during the first ~5s of stimulation and diminished significantly during the later ~25s.
246 Although lower Ca2+ was observed within all astrocytic compartments in AD mice, the most pronounced and
247 significant differences were observed in astrocyte processes (Fig. 1 M & Supplementary Figure 1, p < 1e-4).

248 During the final 2s of the stimulus, peak Ca2+ release was significantly lower in AD mice relative to WT mice
249 for all astrocyte compartments (Fig.s1 J-M, soma $p = 1e-4$, endfeet $p = 7e-4$, processes $p < 1e-4$). Our
250 observations indicate a compartmentalized influence of AD pathology to astrocyte Ca2+.

251 To examine how amyloid pathology and associated hyperactive astrocytes affects hemodynamics in smaller
252 vessels, we performed rapid two-photon line scan measurements to measure capillary diameter and red blood
253 cell speed. Vessel diameter was downsampled to a rate of 20Hz. Vessel dilation in laterally-oriented arteriole
254 branches and capillary branches extending from the downward penetrating arteriole (1st order to 4th order) were
255 measured. We found significant differences in stimulus-induced arteriole dilation between AD and WT mice
256 in response to 3 second stimulus. In capillaries, we observed no differences in dilation between AD and WT
257 for either stimulus duration (supplementary Figure 1).

258

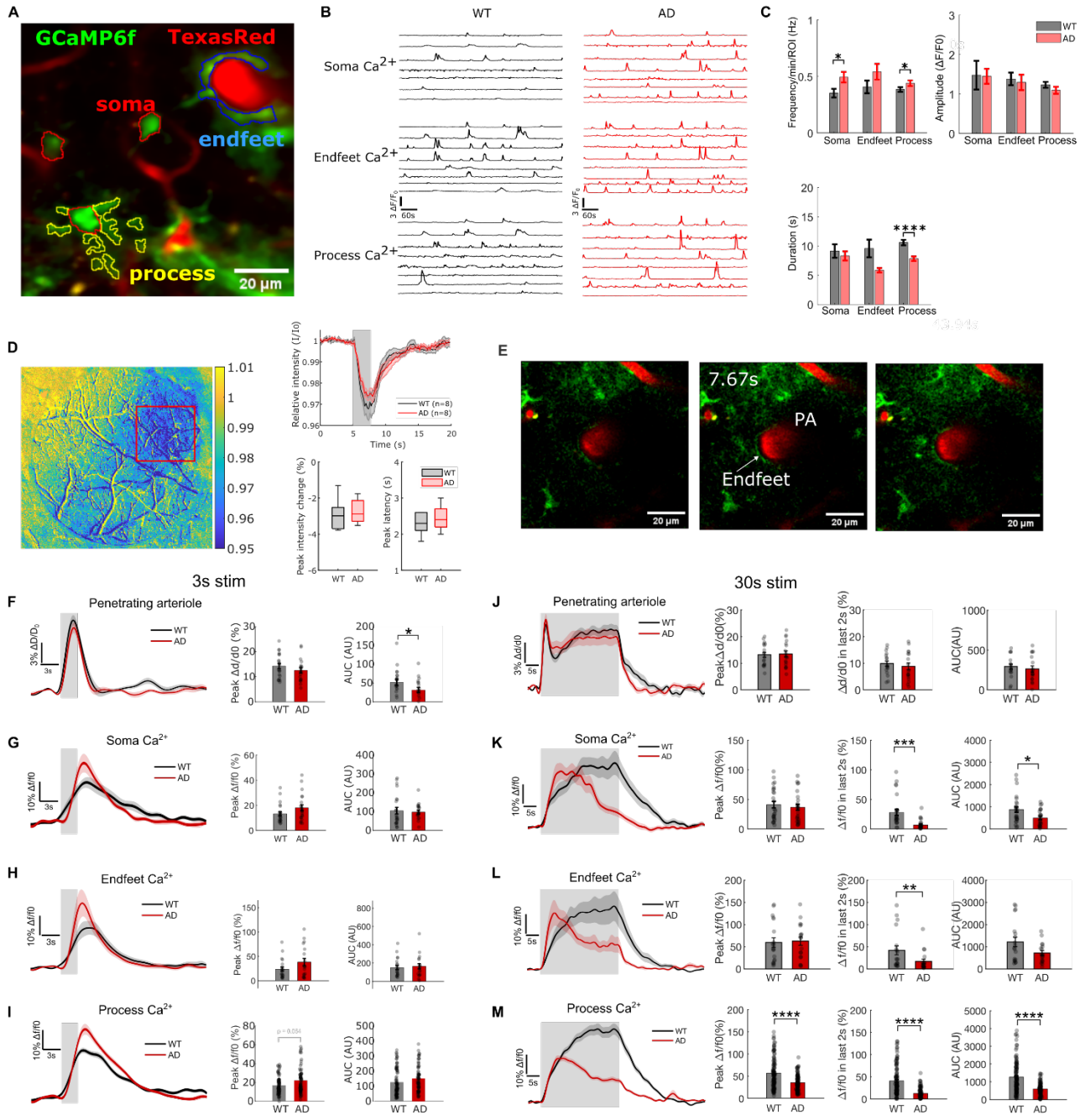

Figure 1. Spontaneous astrocyte Ca2+ and sustained sensory stimulation in AD and WT mice barrel cortex. (A) 2D, raster scan image showing vasculature labelled with Texas-Red and astrocytes expressing GCaMP6f. Annotated regions are soma (red), endfeet (blue), and process (magenta). **(B)** Representative measurements of spontaneous Ca^{2+} release in cortical astrocytes cell compartments recorded for 10 mins. **(C)** Amplitude, Frequency and Duration of Ca^{2+} spikes at different astrocyte ROIs. **(D)** OISI measurement of cerebral hemodynamics in response to 3s whisker stimulation in left barrel cortex in WT and AD mice. **(E)** Representative two-photon raster scan images of diving arteriole dilation and astrocyte Ca^{2+} release during whisker stimulation trials. **(F-I):** Trial-averaged profiles of arteriole dilation and astrocyte Ca^{2+} release in response to 3s whisker stimulation and quantification of the peak response. **(J-L):** Trial-averaged profiles of arteriole dilation and astrocyte Ca^{2+} release in response to 30s whisker

stimulation and the quantification of the peak response. Difference between WT and AD were tested using rank-sum test.

3.2 LPS-induced inflammation reduces spontaneous astrocyte Ca2+ and impairs neurovascular coupling

To evaluate how systemic inflammation alters astrocyte's Ca2+ signaling and its contributions to CBF regulation, animals underwent a prolonged 14-day LPS-induced inflammation challenge. We used 2-photon imaging to measure astrocyte Ca2+ dynamics and microvascular dilation under resting-state conditions and during functional hyperemia in awake AD and WT mice. The same imaging fields of view were imaged on days 0, 7, and 14 of the LPS challenge.

Fig. 2A displays example measurements of resting-state, spontaneous Ca2+ release from astrocytic compartments over the course of the 14-day inflammatory challenge. Similar to pre-LPS resting state measurements, raster scanning was performed in ~100 μm^2 cortical regions surrounding penetrating arterioles for 10 min at ~ 4.4 Hz. We observed no discernible differences in cell morphology from days 0 – 14. Dynamic Ca2+ transients were quantified and analyzed from the soma, processes, and endfoot compartments of astrocytes (Figs 2 B &C). During the 14 day period, we observed variations in spontaneous Ca2+ fluctuations in astrocytes in both cohorts, with some cell compartments demonstrating no Ca2+ transients over the 10 minute measurement. Fig 2.D illustrates how the proportion of these 'silent,' quiescent cell compartments changed during the inflammatory period. Among the cells that remained active in both AD and WT cohorts, the frequency of spontaneous Ca2+ spikes progressively lowered during the 14-day period within astrocyte soma and process compartments (figs 2 E&G).

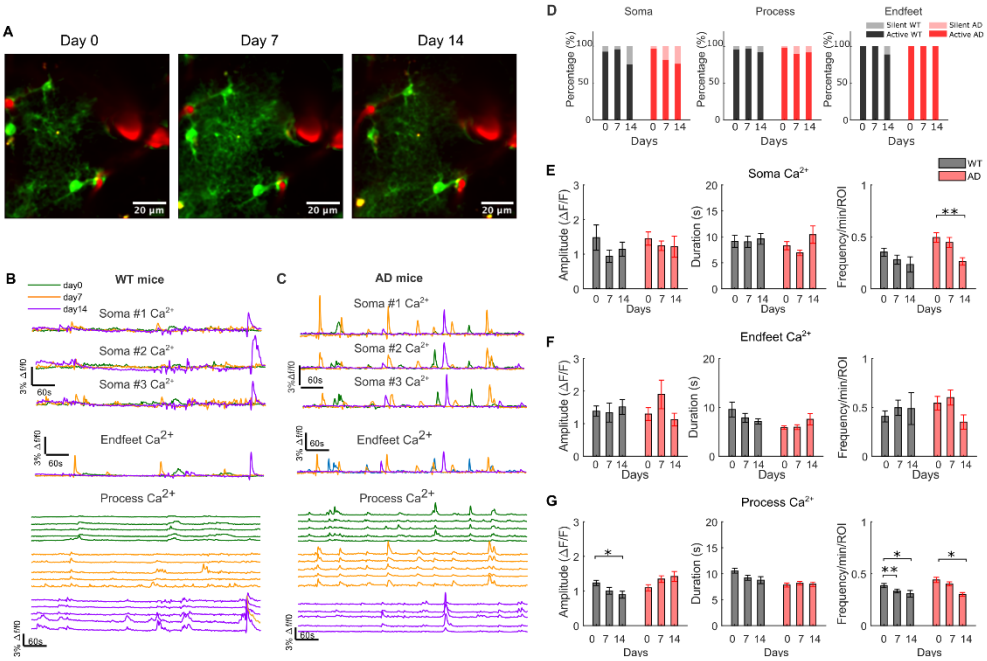

Figure 2. LPS induced inflammation decreased spontaneous Ca2+ release in astrocytes in AD mice cortex. (A) Raster scan image of cortical vasculature and astrocytes at different days during 14-days of LPS-induced systemic inflammation. (B) Spontaneous Ca^{2+} release form astrocyte compartments in WT and AD mice cortex measured on pre-LPS injection (day 0), after 7 and 14 days of LPS injection (day 7 and day14). (D) Variations in spontaneous Ca2+ activity from astrocyte compartments during the 14-day period. (E-G) Quantification of astrocyte Ca2+ spikes under the impact of LPS induced inflammation. Linear mixed effect model was used to test the effect of LPS injection.

To determine whether prolonged systemic inflammation impacts astrocytic contributions to functional hyperemia, we examined arteriolar dilation and astrocyte $Ca2^{+}$ release in response to brief (3s) and sustained (30 s) pneumatic whisker stimulation. For short 3s whisker stimulation, arteriole dilation responses did not change appreciably during the 14-day period for both AD and WT mice (figs 3 A & E), while astrocyte Ca2+ responses varied significantly. In the astrocyte soma of WT mice, Ca2+ release parameters showed reductions in peak response and AUC between days 0 and 7 (fig 3.B, p-val = 0.036 and p-val = 0.047, respectively). For both AD and WT mice, systemic inflammation substantially altered Ca2+ release in astrocyte processes, provoking significant reductions in peak Ca2+ release, AUC, and rise time (figs 3D and 3H), and peak latency in WT mice (supplementary figure 2). Interestingly, the inflammatory threat induced opposing effects in AD and WT mice within astrocyte endfeet. In WT mice, we observed significant increases in peak Ca2+ of endfeet and shorter response duration. Conversely, in AD mice, endfeet showed reduced peak Ca2+ and significantly longer rise times, but longer duration (figs 3 C&G, supplementary figure 2).

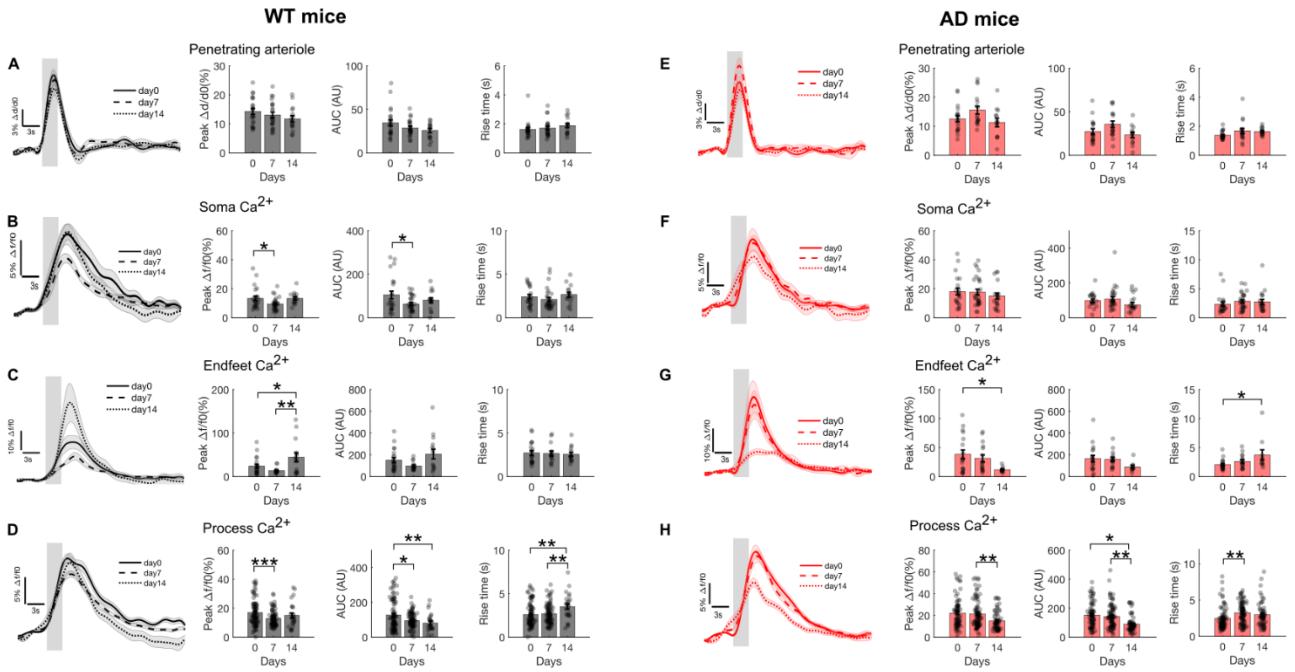

Figure 3. Effect of LPS induced inflammation on penetrating arterial dilation and astrocyte Ca^{2+} release in response to brief whisker 3s stimulation. **(A&E)** Trial-averaged profiles and calculated features of stimulus-induced penetrating arteriole dilation and astrocyte Ca^{2+} release in WT and AD mice on day 0, day7 and day14 of LPS injection. **B-H** Trial-averaged profiles and calculated features of stimulus-induced, compartment-specific astrocyte Ca^{2+} release in WT and AD mice on day 0, day7 and day14 of LPS injection.

For sustained trials with longer 30 second whisker stimulation, the 14-day inflammatory threat provoked more pronounced alterations to WT mice than AD mice. Additionally, more significant alterations were observed in astrocytes than arterioles. In both AD and WT mice, inflammation provoked notable, yet not significant, reductions in arteriole dilation at days 7 and 14. Following stimulus cessation, arterioles returned to their baseline value significantly faster in AD mice, evidenced by the significantly reduced fall time (Supplementary figure 2). In WT mice, peak Ca2+ release, rise times, and peak latency during the entire 30 s stimulation all significantly decreased in soma and processes over the course of the 14 day inflammatory period, and AUC significantly lowered within all compartments. Maximum Ca2+ release during the late phase of stimulation were also significantly reduced in all compartments (fig4 a-d). In AD mice, the inflammatory threat provoked significant reductions in peak Ca2+ release from all astrocyte compartments. The AUC for responses in astrocyte endfeet also decreased significantly during the 14 day period in AD mice, while astrocyte processes showed significant reductions in AUC, peak latency, duration, and maximal fluorescence during the later plateau phase (fig 4 H and supplementary figure 3). Overall, our observations of reduced endfeet Ca2+ release correlate with mildly reduced p.a. dilation at the late phase of stimulation aligns well with prior studies

332 demonstrating that astrocyte Ca2+ help sustain arteriole dilation in response to prolonged functional
333 stimulation [26].

334 Capillaries also regulate cerebral blood flow through pericyte- and astrocyte-mediated dilation [27]. Systemic
335 inflammation increases neutrophils in brain capillaries, causing capillary stalling, and impairs cerebral blood
336 flow [11]. Using rapid line scan measurements, we measured kinetic profiles of stimulus induced vessel
337 dilation in higher order arterioles and capillary branches. Baseline vessel diameters were computed as the mean
338 diameter during the initial 5s prior to whisker stimulation. In WT mice, we observed a significant reduction in
339 baseline capillary diameters for 3rd order capillaries at days 7 and 14 of LPS-induced inflammation
340 (supplementary figure 4).

341 We then examined how inflammation impacts capillary dilation in response to functional stimulation. Trial-
342 averaged line scan measurements indicate that LPS injection yielded smaller capillary responses to sustained
343 stimulation (Supplementary Figure 4); however, we observed few statistically significant changes.

344 We also calculated RBC velocity in high-order (> 3rd-order) capillaries (supplementary figure 4). In WT mice,
345 3s stimulus-evoked RBC velocity (RBCv) change was lower on day 7 relative to baseline. While in AD mice,
346 RBCv was decreased on day 7 but increased on day 14 compared to day 0. Our data further support our
347 observations for vessel dilation in high-order capillaries. Both raster and line scan measurement of capillary
348 dilation and RBC velocity demonstrated that AD mice respond to LPS-induced inflammation differently than
349 WT, with LPS reduced capillary response in WT mice while increase capillary response in AD mice brain.

350

351

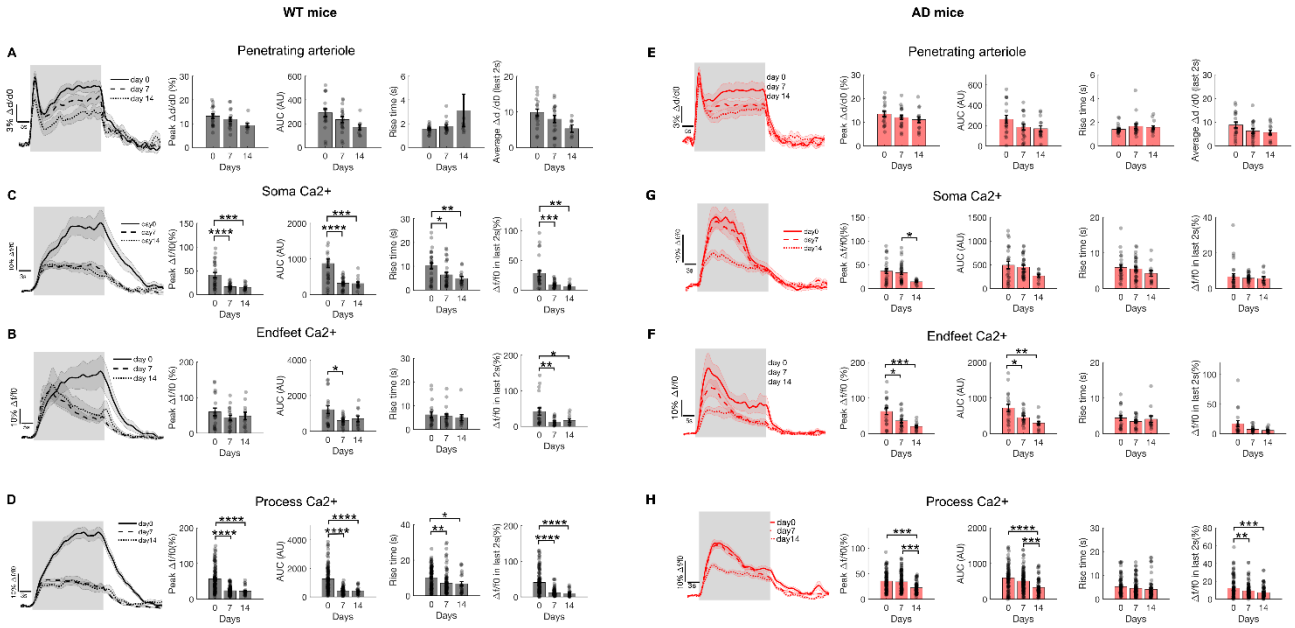

Figure 4. Effect of LPS induced inflammation on cerebral vessel dilation and astrocyte Ca^{2+} release in response to sustained whisker stimulation. **(A-D)** Two-photon raster scanning measurement of 30s whisker stimulation induced penetrating arteriole dilation and astrocyte Ca^{2+} release in WT mice measured on day 0, day 7 and day 14 of LPS injection.

3.5 Ex vivo immunofluorescence analysis of LPS-induced inflammation and $A\beta_{1-42}$ accumulation

To assess neuroinflammation induced after 14 days of LPS injection, we harvested brains from subgroups of mice from each cohort for immunofluorescence (IF) staining of GFAP, Iba-1, and $A\beta_{1-42}$ (n = 3 per cohort). We also analyzed a sham group of mice that received 14 days of saline injections (n=3 for AD, n=2 for WT). Fig. 5A displays representative confocal images of immunofluorescence staining. We quantified GFAP expression in astrocytes and IBA1 expression in microglia by calculating the percentage area of GFAP and IBA1 expressed cells in the confocal images (Fig. 5B). In saline control group, AD mice showed significantly increased GFAP expression in both cortex and hippocampus compared to WT mice, indicating a pre-existing neuroinflammation in AD mice brain. IBA-1 expression is slightly, but not significantly, higher than in AD control compared to WT control mice. After 7 days of LPS injection, GFAP and IBA1 expression in the WT brain both increased, with a statistically significant increase observed in GFAP expression. Interestingly, GFAP expression in AD astrocytes decreased after 7 days of LPS injection while microglial expression of IBA1 increased, suggesting AD astrocytes react to LPS-induced inflammation differently compared to WT animal. Both GFAP and IBA1 expression reduced after 14 days of LPS injection in both cohorts. This trend of recovery agrees well with our previous study exploring cortical oxygen extraction during 14 days of LPS injection [28]. The results could

reflect immune tolerance induced by the repeated injection of low-dose LPS [29–31]. Fig. 5C shows the representative widefield fluorescence imaging of $A\beta_{1\text{-}42}$ in the cortex and hippocampus of AD mice. Strikingly, 14 days of LPS injection yielded reduced $A\beta_{1-42}$ load in AD mice brain, showing statistical significance in cortex and a strong trend in the hippocampus (Fig. 5D). LPS injection induced $A\beta_{1-42}$ reduction was also reported by other studies [32–34]. Higher $A\beta_{1-42}$ load was observed in the cortex compared to hippocampus (Fig. 5D), agreeing well with previous reports in APPswe/PS1dE9 mice [35,36].

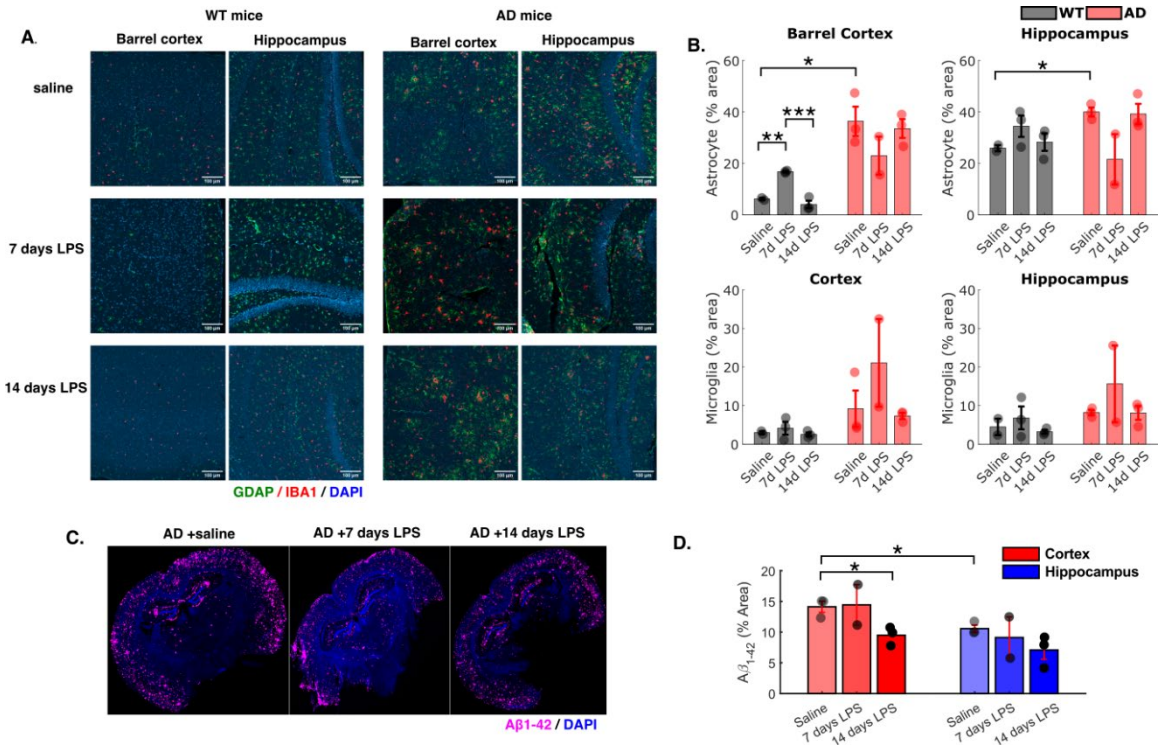

Figure 5. *Ex vivo* immunofluorescence imaging. (A) Immunofluorescence image of $A\beta_{1-42}$In AD mice received 14 days of saline injection (n=3), 7 days of LPS injection (n=2) and 14 days of LPS injection (n=3). (B) Quantification of $A\beta_{1-42}$ in cerebral cortex and hippocampus. $A\beta_{1-42}$ load was quantified using the percentage area. Multiple ROIs were quantified and averaged for each animal. Data shown as the mean $\pm$ sem.(C) Representative confocal immunofluorescence image of GFAP and Iba-1expression in barrel cortex and hippocampus in WT and AD mice. Images were taken under a 10X objective. Scale bar = 100 µm. (D) Percentage area of GFAP and IBA-1 expression in barrel cortex and hippocampus. One-way ANOVA with Tukey's post hoc test was used in (B) and (D) to test the difference between saline, 7 days LPS and 14 days LPS injection. Differences between WT and AD saline control group in (B) and (D) were tested using Student's t test. *p<0.05, **p<0.01, ***p<0.001.

391 ## 4. DISCUSSION

392 Astrocytes perform multifactorial functions for regulating both cerebral energetics and neuroimmunity. We
393 hypothesized that Amyloid deposition in 12-13 month old APP/Swe mice provokes inflammatory alterations
394 that yield disruptions to the mechanisms by which astrocyte Ca2+ modulates cerebral blood flow on both
395 penetrating arterioles and capillaries. We posited that a pronounced systemic inflammatory threat would further
396 exacerbate astrocyte contributions to resting state CBF and functional hyperemia.

397 Under resting state conditions, in the absence of an inflammatory threat, our observations revealed that 12- to
398 13-month-old female APPswe/PS1dE9 mice exhibit increased spontaneous astrocyte Ca^{2+} release and
399 decreased astrocyte Ca^{2+} response to sustained 30s whisker stimulation compared to WT control mice (Figs. 1–
400 3). 14 days of systemic inflammation suppresses both spontaneous and sensory stimulation-evoked astrocyte
401 Ca^{2+} release in the barrel cortex of WT and AD mice and induced moderate changes to vascular response in
402 arterioles and capillaries. Interestingly, LPS treatment also reduced $A\beta_{1-42}$ levels in the cortex and hippocampus
403 of AD mice.

404 ### 4.1 Astrocyte Ca^{2+} signaling in AD

405 Reactive astrocytes with elevated spontaneous Ca^{2+} release had been found in AD mice brains, especially near
406 amyloid plaques [37,38]. Indeed, astrocytes were activated in our 12-month-old APP/P1dE9 mice brain, as
407 indicated by increased GFAP expression in cortex and hippocampus compared with WT mice (Fig. 5) and
408 exhibited increased frequency of spontaneous Ca^{2+} events of cortical astrocytes (Fig. 1). The exact mechanism
409 of aberrant Ca^{2+}in reactive astrocyte is not fully understood. Upregulation of the purinergic and the
410 metabotropic receptors and increased mitochondria Ca^{2+}efflux could explain the increased Ca^{2+} activity in
411 reactive astrocytes [9]. While many studies explored the mechanisms underpinning astrocyte hyperactivity at
412 the resting state, few studies have explored reactive astrocyte Ca^{2+} signaling during functional brain
413 activation [39]. Our observation of reduced astrocyte Ca^{2+}release in AD mice in response to 30s whisker
414 stimulation support prior findings of astrocyte Ca^{2+} activity under sensory-evoked stimulation (Fig. 2, 3). Lines
415 et al also reported increased spontaneous release of Ca^{2+} and decreased hind-paw stimulation evoked responses
416 in astrocytes in 6-month APP/PS1 mice [39]. Interestingly, a study revealed a negative correlation between the
417 amplitude (i.e., absolute change) of the evoked Ca2+ signal and its baseline level [40]. In our AD mice, the
418 declined astrocyte Ca^{2+} response was substantially more pronounced in response to 30s whisker stimulation
419 compared to 3s of stimulation (Fig. 3, supplementary figure 2). The diminished Ca^{2+} release as stimulation
420 persists could be attributed to insufficient Ca^{2+} storage in astrocytes. Lia et al. demonstrated astrocyte
421 hypoactivity in response to ATP and noradrenaline (NA) in 6-month-old PS2APP mice and associated the

422 reduced Ca^{2+} level with reduced endoplasmic reticulum Ca^{2+} concentration [41]. Future studies measuring the
423 store concentration of Ca^{2+} in astrocytes could help to address our hypothesis [42].
424 Conflicting observations of astrocyte Ca^{2+} activity in AD mice model have been reported previously. Shah et
425 al. showed decreased calcium signaling in cingulate astrocytes in APP^{NL-F} mice before the formation of amyloid
426 deposits [8]. The decreased astrocyte Ca^{2+} accounts for increased functional connectivity observed with
427 functional MRI. In 6-month-old PS2APP mice with the presence of Aβ deposit, Lia et al. found declined
428 spontaneous astrocyte cytosolic Ca^{2+} release, and the hypoactivity is independent with Aβ-plaque
429 proximity [41]. The findings regarding astrocyte activity in AD mice vary with the brain region, disease stage,
430 and animal model being studied. Interestingly, our results show mild reductions in vascular response to 3-
431 second and 30-second whisker stimulation in AD mice, indicating only modest differences in stimulus induced
432 blood volume changes between the 2 cohorts.
433
434 **4. 2 Neurovascular coupling in AD brain**
435 Impaired neurovascular coupling has been reported in AD patients and AD mouse models, including Tg2576,
436 J20 mouse and the triple transgenic 3xTg-AD mice [41,43–47]. Our OISI and in vivo imaging with two-photon
437 microscopy showed that 12-month-old female APP/PS1dE9 mice did not exhibit significant alterations in
438 cerebral vascular responses to whisker stimulation (Fig. 1, Supplementary Figure 1). However, dilation in high-
439 order capillaries (diameter < 5 μm) was significantly reduced in AD mice compared to WT (Supplementary fig.
440 1). The results indicate that disrupted neurovascular coupling originates within microvessels in the
441 APP/PS1dE9 mice. Preserved hemodynamic response in cortical arterioles was also reported in the familiar
442 AD mouse model J20 [48,49]. Gutiérrez-Jiménez et al. found reduced resting-state capillary flux and elevated
443 electrical stimulation evoked arteriole dilation and capillary RBC velocity in 18-month-old APPswe/PS1dE9
444 model compared with control mice group [50]. Conversely, early microvascular pathologies were detected in
445 APPswe/PS1dE9 mice with electron microscopy [51] and in 3x-Tg mice with optical coherence
446 tomography [52]. Taken together, our observations and these prior studies indicate that impairments to
447 neurovascular coupling in AD originates in micro vessels at early stages and then spreads to arterioles as the
448 disease progresses.
449
450 **4.3 Neurovascular coupling in systemic inflammation**
451 Previous studies demonstrated that LPS-induced systemic inflammation alters brain hemodynamic responses,
452 including increasing capillary stalling [11,53,54]. Here, we showed that 14 days of LPS-induced systemic
453 inflammation mildly reduced vascular dilation in response to brief 3 s whisker stimulation (Fig. 3,
454 supplementary figure 2), and more pronouncedly reduced hemodynamic response to sustained 30 whisker

455 stimulation in WT and AD mice (Fig. 4, supplementary figure 3). Prior studies focused on the acute effect of a
456 single high-dose LPS injection (>1 mg/kg) and examined the cerebrovascular function within 24 hours after
457 the injection [11,53]. In our study, we used a lower dose of LPS (0.3 mg/kg) and assessed its chronic effects by
458 administering LPS continuously for 14 days and measuring vascular responses to whisker stimulation on days
459 7 and 14. Repeated, daily intraperitoneal injections (i.p.) of low-dose LPS (less than 1 mg/kg) in mice have
460 been shown to induce immune tolerance at the later phases of the challenge. Several groups administrated 4
461 days of daily i.p. injections of low-dose LPS in C57BL/6J mice and 3-month-old APP23 mice [30,29,31]. They
462 measured brain cytokine levels and found increased proinflammatory cytokines (e.g., IL-1β and TNF-α) during
463 the first two days of injections, followed by significantly reduced cytokine levels starting on day 3, despite
464 continued LPS exposure. Meanwhile, anti-inflammatory cytokines, such as IL-10 and TGF-β, increased during
465 the later stages of treatment. These findings suggest a diminishing inflammatory response following the low-
466 dose, repeated systemic administration of LPS. Similarly, our IF result showed unaltered GFAP and Iba-1
467 expression in astrocytes and microglia after 14 days of LPS injection (Fig. 5). Taken together, the diminished
468 inflammatory response could explain why we did not observe detectable alterations in vascular response and
469 glial activation under LPS injection. Additionally, LPS injection did not change the resting-state diameter of
470 cortical penetrating and the precapillary arterioles in either mouse cohort. Only WT mice showed constriction
471 in high-order capillaries after LPS administration (Fig. 4). Our recent study showed that 14 days of low-dose
472 LPS administration did not affect resting state red blood cell flux in capillaries [28]. The reduced resting-state
473 capillary diameter but preserved RBC flux might indicate a reduction in baseline capillary flow.
474
475 **4.4 Systemic inflammation alters astrocyte Ca2+ signaling**
476 While vascular responses appeared to be mildly reduced during prolonged inflammation, astrocyte Ca^{2+} levels
477 were more heavily impacted. Astrocyte Ca^{2+} levels on day 14 showed no signs of recovery in either WT or AD
478 mice and were further decreased in AD mice (Fig. 2). This persistent decline in astrocyte Ca^{2+} release,
479 particularly in AD mice, suggests that other disruptions, such as impaired neuronal activity, may contribute to
480 the observed deficits. Moreover, the reduction in astrocyte Ca^{2+} is linked with reduced $A\beta_{1-42}$ in AD mice cortex
481 and hippocampus (Fig. 5). Many studies showed systemic LPS injection ameliorates amyloid
482 pathology [33,55,32,34]. The involvement of astrocyte Ca^{2+} signaling in this process requires further
483 investigation. Strikingly, in our APP/PS1dE9 mouse model, LPS substantially reduced sensory stimulation-
484 evoked astrocyte Ca^{2+} while only mildly affecting arteriole dilation (Figs. 3 and 4). Instead, capillary dilation
485 was decreased in AD mice (Fig. 4). The role of astrocyte Ca^{2+} in regulating cerebral blood flow during
486 functional hyperemia remains uncertain and widely-debated [6]. Silencing astrocyte Ca^{2+} using CalEx affects
487 arteriole dilation during sustained sensory stimulation, with no impact on brief sensory stimulation. Notably,

488 only the late phase of vessel dilation during sustained stimulation was reduced [26]. Other studies showed
489 astrocyte Ca2+ signaling mediates neurovascular signaling to capillary pericytes but not arterioles [56]. LPS
490 has been shown to cause pericyte loss and microvascular dysfunction [57,58]. Further studies investigating
491 neurovascular coupling in capillary pericytes and astrocyte Ca^{2+} signaling under AD-related inflammation could
492 offer greater insights.
493 Lastly, astrocyte Ca^{2+} also plays a pivotal role in regulating neuronal activity and synaptic plasticity [59]. LPS-
494 induced systemic inflammation causes neuronal hyperexcitability [60,61]. Increased neuronal activity was also
495 reported in the early stages of AD [62]. Our recent study showed that 14 days of systemic injection of LPS
496 increased oxygen extraction in the somatosensory cortex in 8–to 9-month-old APP/PS1dE9 mice and the age-
497 matched control [28]. Therefore, the reduced Ca^{2+} levels in astrocyte soma and processes under AD and LPS
498 may be linked to alterations in neuronal activity during functional brain activation.

499

500 **ACKNOWLEDGMENTS**

501 This work was performed with generous support from the Northeastern College of Engineering and the National
502 Institutes of Health: NIH R01AA27097, NIH R56AG058849, and R21AG085655. We thank Dr. Martin
503 Thunemann and John Jiang from Boston University for their guidance with animal surgery and calcium
504 imaging. We thank the Institute for Chemical Imaging of Living Systems (RRID:SCR_022681) at Northeastern
505 University for consultation and imaging support, and for the assistance of confocal imaging and wide-field
506 fluorescence imaging. We thank Dana-Farber/Harvard Cancer Center in Boston, MA, for the use of the
507 Specialized Histopathology Core, which provided brain slices immunofluorescence staining service. Dana-
508 Farber/Harvard Cancer Center is supported in part by an NCI Cancer Center Support Grant # NIH 5 P30
509 CA06516.

510

511 ## References

512 1. V. Calsolaro and P. Edison, "Neuroinflammation in Alzheimer's disease: Current evidence and future directions,"
513 Alzheimer's & Dementia **12**, 719–732 (2016).
514 2. M. T. Heneka, M. J. Carson, J. E. Khoury, G. E. Landreth, F. Brosseron, D. L. Feinstein, A. H. Jacobs, T. Wyss-
515 Coray, J. Vitorica, R. M. Ransohoff, K. Herrup, S. A. Frautschy, B. Finsen, G. C. Brown, A. Verkhratsky, K.
516 Yamanaka, J. Koistinaho, E. Latz, A. Halle, G. C. Petzold, T. Town, D. Morgan, M. L. Shinohara, V. H. Perry, C.
517 Holmes, N. G. Bazan, D. J. Brooks, S. Hunot, B. Joseph, N. Deigendesch, O. Garaschuk, E. Boddeke, C. A.
518 Dinarello, J. C. Breitner, G. M. Cole, D. T. Golenbock, and M. P. Kummer, "Neuroinflammation in Alzheimer's
519 disease," The Lancet Neurology **14**, 388–405 (2015).
520 3. C. Iadecola, "Neurovascular regulation in the normal brain and in Alzheimer's disease," Nat Rev Neurosci **5**, 347–
521 360 (2004).
522 4. B. V. Zlokovic, "Neurovascular pathways to neurodegeneration in Alzheimer's disease and other disorders," Nat
523 Rev Neurosci **12**, 723–738 (2011).
524 5. E. Colombo and C. Farina, "Astrocytes: Key Regulators of Neuroinflammation," Trends in Immunology **37**, 608–
525 620 (2016).
526 6. A. Lia, A. Di Spiezio, M. Speggiorin, and M. Zonta, "Two decades of astrocytes in neurovascular coupling," Front.
527 Netw. Physiol. **3**, 1162757 (2023).
528 7. G. R. Frost and Y.-M. Li, "The role of astrocytes in amyloid production and Alzheimer's disease," Open Biol. **7**,
529 170228 (2017).
530 8. D. Shah, W. Gsell, J. Wahis, E. S. Luckett, T. Jamoulle, B. Vermaercke, P. Preman, D. Moechars, V. Hendrickx, T.
531 Jaspers, K. Craessaerts, K. Horré, L. Wolfs, M. Fiers, M. Holt, D. R. Thal, Z. Callaerts-Vegh, R. D'Hooge, R.
532 Vandenberghe, U. Himmelreich, V. Bonin, and B. De Strooper, "Astrocyte calcium dysfunction causes early
533 network hyperactivity in Alzheimer's disease," Cell Reports **40**, 111280 (2022).
534 9. E. Shigetomi, K. Saito, F. Sano, and S. Koizumi, "Aberrant Calcium Signals in Reactive Astrocytes: A Key Process
535 in Neurological Disorders," Int J Mol Sci **20**, 996 (2019).
536 10. A. Verkhratsky, "Astroglial Calcium Signaling in Aging and Alzheimer's Disease," Cold Spring Harb Perspect Biol
537 **11**, a035188 (2019).
538 11. S. K. Fruekilde, C. J. Bailey, K. L. Lambertsen, B. H. Clausen, J. Carlsen, N. Xu, K. R. Drasbek, and E. Gutiérrez-
539 Jiménez, "Disturbed microcirculation and hyperaemic response in a murine model of systemic inflammation," J
540 Cereb Blood Flow Metab 0271678X2211122 (2022).
541 12. L. E. Evans, J. L. Taylor, C. J. Smith, H. A. T. Pritchard, A. S. Greenstein, and S. M. Allan, "Cardiovascular
542 comorbidities, inflammation, and cerebral small vessel disease," Cardiovascular Research cvab284 (2021).
543 13. S. B. Sankar, A. F. Pybus, A. Liew, B. Sanders, K. J. Shah, L. B. Wood, and E. M. Buckley, "Low cerebral blood
544 flow is a non-invasive biomarker of neuroinflammation after repetitive mild traumatic brain injury," Neurobiol Dis
545 **124**, 544–554 (2019).

546 14. C. R. A. Batista, G. F. Gomes, E. Candelario-Jalil, B. L. Fiebich, and A. C. P. de Oliveira, "Lipopolysaccharide-
547 Induced Neuroinflammation as a Bridge to Understand Neurodegeneration," IJMS **20**, 2293 (2019).
548 15. L. Qin, X. Wu, M. L. Block, Y. Liu, G. R. Breese, J.-S. Hong, D. J. Knapp, and F. T. Crews, "Systemic LPS causes
549 chronic neuroinflammation and progressive neurodegeneration," Glia **55**, 453–462 (2007).
550 16. J. L. Jankowsky, D. J. Fadale, J. Anderson, G. M. Xu, V. Gonzales, N. A. Jenkins, N. G. Copeland, M. K. Lee, L.
551 H. Younkin, S. L. Wagner, S. G. Younkin, and D. R. Borchelt, "Mutant presenilins specifically elevate the levels
552 of the 42 residue β-amyloid peptide in vivo: evidence for augmentation of a 42-specific γ secretase," Human
553 Molecular Genetics **13**, 159–170 (2004).
554 17. K. Kılıç, M. Desjardins, J. Tang, M. Thunemann, S. Sunil, Ş. E. Erdener, D. D. Postnov, D. A. Boas, and A. Devor,
555 "Chronic Cranial Windows for Long Term Multimodal Neurovascular Imaging in Mice," Front. Physiol. **11**,
556 612678 (2021).
557 18. R. L. Lowery and A. K. Majewska, "Intracranial Injection of Adeno-associated Viral Vectors," JoVE 2140 (2010).
558 19. A. Y. Shih, J. D. Driscoll, P. J. Drew, N. Nishimura, C. B. Schaffer, and D. Kleinfeld, "Two-Photon Microscopy as
559 a Tool to Study Blood Flow and Neurovascular Coupling in the Rodent Brain," J Cereb Blood Flow Metab **32**,
560 1277–1309 (2012).
561 20. E. A. Pnevmatikakis and A. Giovannucci, "NoRMCorre: An online algorithm for piecewise rigid motion correction
562 of calcium imaging data," Journal of Neuroscience Methods **291**, 83–94 (2017).
563 21. R. Srinivasan, B. S. Huang, S. Venugopal, A. D. Johnston, H. Chai, H. Zeng, P. Golshani, and B. S. Khakh, "Ca2+
564 signaling in astrocytes from Ip3r2−/− mice in brain slices and during startle responses in vivo," Nat Neurosci **18**,
565 708–717 (2015).
566 22. J. L. Stobart, K. D. Ferrari, M. J. P. Barrett, M. J. Stobart, Z. J. Looser, A. S. Saab, and B. Weber, "Long-term In
567 Vivo Calcium Imaging of Astrocytes Reveals Distinct Cellular Compartment Responses to Sensory Stimulation,"
568 Cerebral Cortex **28**, 184–198 (2018).
569 23. J. N. Haidey, G. Peringod, A. Institoris, K. A. Gorzo, W. Nicola, M. Vandal, K. Ito, S. Liu, C. Fielding, F. Visser,
570 M. D. Nguyen, and G. R. Gordon, "Astrocytes regulate ultra-slow arteriole oscillations via stretch-mediated
571 TRPV4-COX-1 feedback," Cell Reports **36**, 109405 (2021).
572 24. M. J. P. Barrett, K. D. Ferrari, J. L. Stobart, M. Holub, and B. Weber, "CHIPS: an Extensible Toolbox for Cellular
573 and Hemodynamic Two-Photon Image Analysis," Neuroinform **16**, 145–147 (2018).
574 25. P. Y. Chhatbar and P. Kara, "Improved blood velocity measurements with a hybrid image filtering and iterative
575 Radon transform algorithm," Front. Neurosci. **7**, (2013).
576 26. A. Institoris, M. Vandal, G. Peringod, C. Catalano, C. H. Tran, X. Yu, F. Visser, C. Breiteneder, L. Molina, B. S.
577 Khakh, M. D. Nguyen, R. J. Thompson, and G. R. Gordon, "Astrocytes amplify neurovascular coupling to
578 sustained activation of neocortex in awake mice," Nat Commun **13**, 7872 (2022).
579 27. S. Grubb, M. Lauritzen, and C. Aalkjær, "Brain capillary pericytes and neurovascular coupling," Comparative
580 Biochemistry and Physiology Part A: Molecular & Integrative Physiology **254**, 110893 (2021).

581 28. C. Liu, A. Cárdenas-Rivera, S. Teitelbaum, A. Birmingham, M. Alfadhel, and M. A. Yaseen, "Neuroinflammation
582 increases oxygen extraction in a mouse model of Alzheimer's disease," Alz Res Therapy **16**, 78 (2024).
583 29. J. Kim, O. Sullivan, K. Lee, J. Jao, J. Tamayo, A. M. Madany, B. Wong, P. Ashwood, and A. V. Ciernia, "Repeated
584 LPS induces training and tolerance of microglial responses across brain regions," J Neuroinflammation **21**, 233
585 (2024).
586 30. A.-C. Wendeln, K. Degenhardt, L. Kaurani, M. Gertig, T. Ulas, G. Jain, J. Wagner, L. M. Häsler, K. Wild, A.
587 Skodras, T. Blank, O. Staszewski, M. Datta, T. P. Centeno, V. Capece, Md. R. Islam, C. Kerimoglu, M.
588 Staufenbiel, J. L. Schultze, M. Beyer, M. Prinz, M. Jucker, A. Fischer, and J. J. Neher, "Innate immune memory in
589 the brain shapes neurological disease hallmarks," Nature **556**, 332–338 (2018).
590 31. D. M. Norden, P. J. Trojanowski, E. Villanueva, E. Navarro, and J. P. Godbout, "Sequential activation of microglia
591 and astrocyte cytokine expression precedes increased iba‐1 or GFAP immunoreactivity following systemic
592 immune challenge," Glia **64**, 300–316 (2016).
593 32. C. Thygesen, L. Ilkjær, S. J. Kempf, A. L. Hemdrup, C. U. von Linstow, A. A. Babcock, S. Darvesh, M. R. Larsen,
594 and B. Finsen, "Diverse Protein Profiles in CNS Myeloid Cells and CNS Tissue From Lipopolysaccharide- and
595 Vehicle-Injected APPSWE/PS1ΔE9 Transgenic Mice Implicate Cathepsin Z in Alzheimer's Disease," Front. Cell.
596 Neurosci. **12**, 397 (2018).
597 33. T. M. Malm, M. Koistinaho, M. Pärepalo, T. Vatanen, A. Ooka, S. Karlsson, and J. Koistinaho, "Bone-marrow-
598 derived cells contribute to the recruitment of microglial cells in response to β-amyloid deposition in APP/PS1
599 double transgenic Alzheimer mice," Neurobiology of Disease **18**, 134–142 (2005).
600 34. C. Jendresen, A. Digre, H. Cui, X. Zhang, I. Vlodavsky, J.-P. Li, and L. N. G. Nilsson, "Systemic LPS-induced Aβ-
601 solubilization and clearance in AβPP-transgenic mice is diminished by heparanase overexpression," Sci Rep **9**,
602 4600 (2019).
603 35. C. U. Von Linstow, J. Waider, M. Grebing, A. Metaxas, K. P. Lesch, and B. Finsen, "Serotonin augmentation
604 therapy by escitalopram has minimal effects on amyloid-β levels in early-stage Alzheimer's-like disease in mice,"
605 Alz Res Therapy **9**, 74 (2017).
606 36. A. Willuweit, M. Schöneck, S. Schemmert, P. Lohmann, S. Bremen, D. Honold, N. Burda, N. Jiang, S. Beer, J.
607 Ermert, D. Willbold, N. J. Shah, and K.-J. Langen, "Comparison of the Amyloid Load in the Brains of Two
608 Transgenic Alzheimer's Disease Mouse Models Quantified by Florbetaben Positron Emission Tomography,"
609 Front. Neurosci. **15**, 699926 (2021).
610 37. K. V. Kuchibhotla, C. R. Lattarulo, B. T. Hyman, and B. J. Bacskai, "Synchronous Hyperactivity and Intercellular
611 Calcium Waves in Astrocytes in Alzheimer Mice," Science **323**, 1211–1215 (2009).
612 38. A. Delekate, M. Füchtemeier, T. Schumacher, C. Ulbrich, M. Foddis, and G. C. Petzold, "Metabotropic P2Y1
613 receptor signalling mediates astrocytic hyperactivity in vivo in an Alzheimer's disease mouse model," Nat
614 Commun **5**, 5422 (2014).
615 39. J. Lines, A. M. Baraibar, C. Fang, E. D. Martin, J. Aguilar, M. K. Lee, A. Araque, and P. Kofuji, "Astrocyte‐
616 neuronal network interplay is disrupted in Alzheimer's disease mice," Glia **70**, 368–378 (2022).

617 40. C. M. King, K. Bohmbach, D. Minge, A. Delekate, K. Zheng, J. Reynolds, C. Rakers, A. Zeug, G. C. Petzold, D. A.
618 Rusakov, and C. Henneberger, "Local Resting Ca2+ Controls the Scale of Astroglial Ca2+ Signals," Cell Reports
619 **30**, 3466-3477.e4 (2020).
620 41. A. Lia, G. Sansevero, A. Chiavegato, M. Sbrissa, D. Pendin, L. Mariotti, T. Pozzan, N. Berardi, G. Carmignoto, C.
621 Fasolato, and M. Zonta, "Rescue of astrocyte activity by the calcium sensor STIM1 restores long-term synaptic
622 plasticity in female mice modelling Alzheimer's disease," Nat Commun **14**, 1590 (2023).
623 42. J. Suzuki, K. Kanemaru, K. Ishii, M. Ohkura, Y. Okubo, and M. Iino, "Imaging intraorganellar Ca2+ at subcellular
624 resolution using CEPIA," Nat Commun **5**, 4153 (2014).
625 43. Y. Iturria-Medina, R. C. Sotero, P. J. Toussaint, J. M. Mateos-Pérez, A. C. Evans, and Alzheimer's Disease
626 Neuroimaging Initiative, "Early role of vascular dysregulation on late-onset Alzheimer's disease based on
627 multifactorial data-driven analysis," Nat Commun **7**, 11934–11934 (2016).
628 44. S. Tarantini, C. H. T. Tran, G. R. Gordon, Z. Ungvari, and A. Csiszar, "Impaired neurovascular coupling in aging
629 and Alzheimer's disease: Contribution of astrocyte dysfunction and endothelial impairment to cognitive decline,"
630 Experimental Gerontology **94**, 52–58 (2017).
631 45. L. Park, J. Zhou, K. Koizumi, G. Wang, A. Anfray, S. J. Ahn, J. Seo, P. Zhou, L. Zhao, S. Paul, J. Anrather, and C.
632 Iadecola, "tPA Deficiency Underlies Neurovascular Coupling Dysfunction by Amyloid-β," J. Neurosci. **40**, 8160–
633 8173 (2020).
634 46. L. Li, X.-K. Tong, M. Hosseini Kahnouei, D. Vallerand, E. Hamel, and H. Girouard, "Impaired Hippocampal
635 Neurovascular Coupling in a Mouse Model of Alzheimer's Disease," Front. Physiol. **12**, 715446 (2021).
636 47. C. F. Lourenço, A. Ledo, R. M. Barbosa, and J. Laranjinha, "Neurovascular uncoupling in the triple transgenic
637 model of Alzheimer's disease: Impaired cerebral blood flow response to neuronal-derived nitric oxide signaling,"
638 Experimental Neurology **291**, 36–43 (2017).
639 48. P. S. Sharp, K. E. Ameen-Ali, L. Boorman, S. Harris, S. Wharton, C. Howarth, O. Shabir, P. Redgrave, and J.
640 Berwick, "Neurovascular coupling preserved in a chronic mouse model of Alzheimer's disease: Methodology is
641 critical," J Cereb Blood Flow Metab **40**, 2289–2303 (2020).
642 49. O. Shabir, B. Pendry, L. Lee, B. Eyre, P. S. Sharp, M. A. Rebollar, D. Drew, C. Howarth, P. R. Heath, S. B.
643 Wharton, S. E. Francis, and J. Berwick, "Assessment of neurovascular coupling and cortical spreading depression
644 in mixed mouse models of atherosclerosis and Alzheimer's disease," eLife **11**, e68242 (2022).
645 50. E. Gutiérrez-Jiménez, H. Angleys, P. M. Rasmussen, M. J. West, L. Catalini, N. K. Iversen, M. S. Jensen, S.
646 Frische, and L. Østergaard, "Disturbances in the control of capillary flow in an aged APPswe/PS1ΔE9 model of
647 Alzheimer's disease," Neurobiology of Aging **62**, 82–94 (2018).
648 51. P. Kelly, P. Denver, S. C. Satchell, M. Ackermann, M. A. Konerding, and C. A. Mitchell, "Microvascular
649 ultrastructural changes precede cognitive impairment in the murine APPswe/PS1dE9 model of Alzheimer's
650 disease," Angiogenesis **20**, 567–580 (2017).

651 52. K. W. Walek, S. Stefan, J.-H. Lee, P. Puttigampala, A. H. Kim, S. W. Park, P. J. Marchand, F. Lesage, T. Liu, Y.-
652 W. A. Huang, D. A. Boas, C. Moore, and J. Lee, "Near-lifespan longitudinal tracking of brain microvascular
653 morphology, topology, and flow in male mice," Nat Commun **14**, 2982 (2023).
654 53. G. Brezzo, J. Simpson, K. E. Ameen-Ali, J. Berwick, and C. Martin, "Acute effects of systemic inflammation upon
655 the neuro-glial-vascular unit and cerebrovascular function," Brain, Behavior, & Immunity - Health **5**, 100074
656 (2020).
657 54. B. Rosengarten, S. Wolff, S. Klatt, and R. T. Schermuly, "Effects of inducible nitric oxide synthase inhibition or
658 norepinephrine on the neurovascular coupling in an endotoxic rat shock model," Crit Care **13**, R139 (2009).
659 55. M. Go, J. Kou, J.-E. Lim, J. Yang, and K. Fukuchi, "Microglial response to LPS increases in wild-type mice during
660 aging but diminishes in an Alzheimer's mouse model: Implication of TLR4 signaling in disease progression,"
661 Biochemical and Biophysical Research Communications **479**, 331–337 (2016).
662 56. A. Mishra, J. P. Reynolds, Y. Chen, A. V. Gourine, D. A. Rusakov, and D. Attwell, "Astrocytes mediate
663 neurovascular signaling to capillary pericytes but not to arterioles," Nat Neurosci **19**, 1619–1627 (2016).
664 57. H. Zeng, X. He, Q. Tuo, D. Liao, G. Zhang, and J. Chen, "LPS causes pericyte loss and microvascular dysfunction
665 via disruption of Sirt3/angiopoietins/Tie-2 and HIF-2α/Notch3 pathways," Sci Rep **6**, 20931 (2016).
666 58. T. P. Carvalho, F. A. O. Toledo, D. F. A. Bautista, M. F. Silva, J. B. S. Oliveira, P. A. Lima, F. B. Costa, N. Q.
667 Ribeiro, J.-Y. Lee, A. Birbrair, T. A. Paixão, R. M. Tsolis, and R. L. Santos, "Pericytes modulate endothelial
668 inflammatory response during bacterial infection," mBio **15**, e03252-23 (2024).
669 59. N. Bazargani and D. Attwell, "Astrocyte calcium signaling: the third wave," Nat Neurosci **19**, 182–189 (2016).
670 60. R. Doenlen, U. Krügel, T. Wirth, C. Riether, A. Engler, G. Prager, H. Engler, M. Schedlowski, and G. Pacheco-
671 López, "Electrical activity in rat cortico-limbic structures after single or repeated administration of
672 lipopolysaccharide or staphylococcal enterotoxin B," Proc. R. Soc. B. **278**, 1864–1872 (2011).
673 61. K. Odoj, B. Brawek, N. Asavapanumas, N. Mojtahedi, M. T. Heneka, and O. Garaschuk, "In vivo mechanisms of
674 cortical network dysfunction induced by systemic inflammation," Brain, Behavior, and Immunity **96**, 113–126
675 (2021).
676 62. H. Targa Dias Anastacio, N. Matosin, and L. Ooi, "Neuronal hyperexcitability in Alzheimer's disease: what are the
677 drivers behind this aberrant phenotype?," Transl Psychiatry **12**, 257 (2022).

678

679